Tellus (1982), *34*, 429–439

The evolution of a sub-cloud layer structure associated with a severe storm—a case study

By SOON-UNG PARK and DHIRENDRA N. SIKDAR, *Atmospheric Sciences, University of Wisconsin-Milwaukee, Milwaukee, WI 53201, U.S.A.*

(Manuscript received March 2; in final form December 17, 1981)

ABSTRACT

Using meteorological tower data from the NSSL (National Severe Storms Laboratory) in Oklahoma, evolutionary characteristics of a turbulent boundary layer are examined during the pre-storm and storm periods on May 20, 1977. Analyses include the vertical profiles of mean and turbulent quantities of wind, temperature, mixing ratio, momentum, and sensible and latent heat fluxes for the pre-storm and storm periods. The results indicate that a substantial modification occurs in the character of the lower boundary layer in each of these periods.

In the pre-storm (no precipitation) the boundary layer is characterized by a weakly stratified mixed layer; the energy source is found located in the surface layer, and the dominant term in the turbulent budget equation is shear generation. During the storm period, the mixed layer yields to a stable boundary layer, due to a net cooling effect associated with the storm-scale motions at lower levels. The structure of the boundary layer is mainly determined by the storm-scale fluxes originating from the cloud layer.

1. Introduction

Similarity theory and experimental data have given us a reasonably complete picture of a steady, horizontally homogeneous surface layer (Wyngaard and Cote, 1971; Businger et al., 1971; others). However, the turbulent quantities above the surface layer are not yet well understood, especially under a severe storm situation. In recent years a few aircraft measurements of turbulent quantities above the surface layer have been reported for undisturbed conditions (Lenschow, 1970; Pennell and Le Mone, 1971; Coulman and Warner, 1977). Under a slightly convective situation the boundary layer structure depends mainly on the surface fluxes of heat and momentum and a downward heat flux corresponding to the conversion of turbulent kinetic energy to potential energy at the layer-top (Ball, 1960; Carson, 1973; Tennekes, 1973; Mahrt and Lenschow, 1976). Some tethered balloon soundings gathered during the 1969 BOMEX reveal that a substantial change occurs in the character and stratification of the lower subcloud layer from the undisturbed to disturbed states (Echternacht and Garstang, 1976); for the disturbed state, the subcloud layer structure seems to be determined by the forcing from the cloud layer. It is not clear yet as to how the cloud layer feedback is related to stability changes in the subcloud layer, especially in a severe storm situation and also what scales of motions are involved in the cloud to subcloud layer exchange processes.

In this paper we describe the evolution of a boundary layer structure based on measurements of winds, temperature and mixing ratio made from the KTVY tower at the NSSL (National Severe Storms Laboratory) on 20 May 1977, when the tower experienced a passing severe thunderstorm accompanied by heavy precipitation. This could be identified from the NSSL radar echoes (Park and Sikdar, 1980). The analyses of metereological data include two periods: pre-storm and storm, based on precipitation observations at the tower and the radar echo movement. Each period covers about 40 min. The data sampling interval was 10 s. Both

0040-2826/82/050429-11$02.50/0

the mean and turbulent quantities are computed for the two periods and turbulent kinetic energy budget terms are evaluated and compared. The sampling frequency was inadequate for evaluating the dissipation and the pressure transport terms.

2. Tower sensors and data processing

The KTVY tower, located at 35°42.2′N, 97°29.4′W, is surrounded by gently rolling terrain with no more than 40 m change in elevation within a 4 km radius of the tower (Goff and Zittel, 1974). The tower was equipped at seven levels (surface (7 m), 26, 45, 89, 177, 266 and 444 m) with horizontal wind and temperature sensors, vertical wind sensors at six levels above surface and wet-bulb temperature sensors at four levels (surface, 89, 266 and 444 m). A raingauge was located at the surface and two pressure sensors were available; one at the surface and the other at the top level (444 m). Digital data, recorded at about 10 s intervals on magnetic tape, have been used for this analysis. Details on the TV tower instrumentation and the accuracy of measurements are available in Carter (1970) and Goff and Zittel (1974). The NSSL tower data have been used in recent years by numerous investigators (e.g. Charba, 1974; Colmer, 1971) to study the vertical thermodynamic and dynamic structure of thunderstorm gust fronts.

Pressure at four levels (surface, 89, 266 and 444 m) was obtained by linear interpolation from pressures measured at two levels. These interpolated values were used to calculate moisture data from wet-bulb temperatures at four levels. The vapor pressure was calculated from wet-bulb temperature using

$$e = e_s(T_w) - \gamma(T - T_w), \tag{1}$$

where e is the vapor pressure, $e_s(T_w)$ the saturation vapor pressure at wet-bulb temperature (T_w), T the air temperature, and where γ is defined by

$$\gamma = 6.61 \times 10^{-4} (1 + 1.15 \times 10^{-3} T_w) \times p$$

T_w is the wet-bulb temperature (°C) and p is pressure (mb). Mixing ratio at four levels (surface, 89, 266 and 444 m) is calculated using the computed e values from Eq. (1).

Oklahoma City (OKC) radar is used to measure the speed and direction of the storm (Park and Sikdar, 1980), which produced heavy precipitation at the tower. The storm was moving from the south-southwest of OKC at a speed 20 m s^{-1}. The sky over NSSL network was overcast with high and middle clouds during the pre-storm period (for synoptic details see Park and Sikdar, 1980). To examine changes of field variables with respect to the storm movement the coordinate system is transformed. In the right-hand coordinate system, the x-axis, which defines the u component, is in the direction of the storm movement; the y-axis which defines the v component, is perpendicular to x; and the z-axis which defines the w component is upright. The classification of two observation periods is based upon raingauge and radar observations of precipitation at the tower.

(1) Pre-storm period; Before the precipitation occurrence (1737 to 1817 CST).

(2) Storm period; The heavy precipitation period (1817 to 1857 CST).

Fig. 1. shows the 3 min average precipitation rate at the tower. Rain started at around 1814 CST, reached a peak at 1850 CST and sharply decreased thereafter. During the storm period the maximum precipitation rate is 6.2 cm/h. Also seen in this profile is an indication of 10–12 min periodicity in the rain intensification.

3. Observational results

3.1 *Mean quantities*

The observed values of mean potential temperature $\bar{\theta}$, mixing ratio $\bar{q}$ and virtual potential temperature θ_v which represent the combined effect of temperature and water vapor on atmospheric stability are illustrated in Fig. 2 for the two periods.

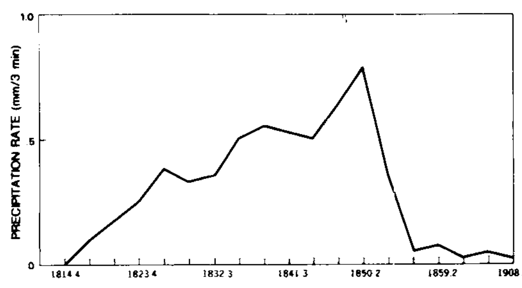

Fig. 1. Three min. average precipitation rate at the KTVY tower. Time 1814.4 means 18 hours and 14.4 minutes in CST.

Both the potential temperature (Fig. 2a) and the virtual potential temperature (Fig. 2b) show a strong stable region below 89 m with a mixed layer above the level during the pre-storm period. However, the whole boundary layer becomes more stabilized during the storm period with an intense cooling at lower levels and a slight cooling at upper levels. The mixing ratio (Fig. 2c) indicates a negative gradient with height in the whole layer for both periods; a significant drying at upper levels, while moistening near the surface in the storm period. Both the increase of mixing ratio and the decrease of temperature during the storm-period indicate the effect of evaporative cooling near the surface, but at upper levels, this effect seems not as important compared to that of the cold downdraft in the heavy precipitation.

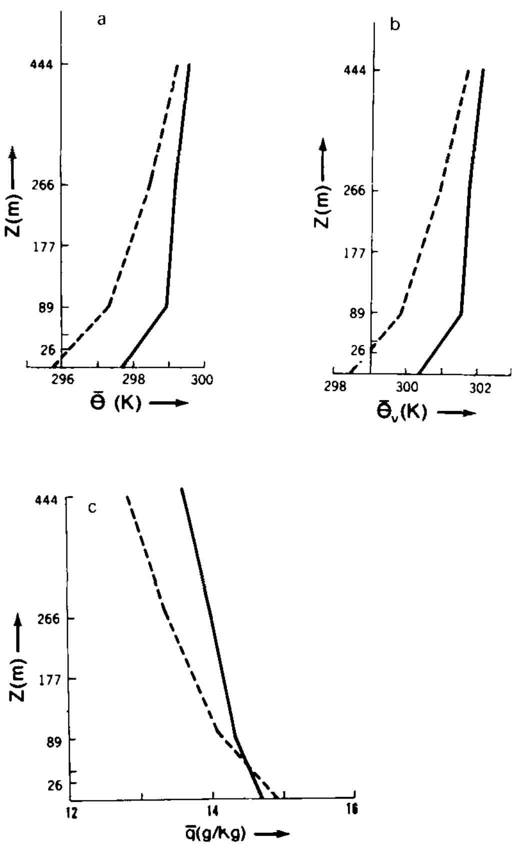

Fig. 2. Vertical profiles of mean (a) potential temperature, (b) virtual potential temperature and (c) mixing ratio for the periods of pre-storm (——) and storm (---).

The observed mean wind profile $\bar{u}$ is presented in Fig. 3 for both periods. In the $\bar{u}$ profiles during the storm period a momentum mixing is seen above the surface layer, resulting in a substantial decrease in vertical wind shear, but for the pre-storm period the momentum is not well mixed despite the potential temperature profile in Fig. 2a, where a mixed layer is seen in the pre-storm period. The momentum mixing in the storm period may be attributed to the strong updrafts and downdrafts in intense convection.

3.2 *Turbulence quantities*

In Fig. 4 the observed winds are plotted at two levels (surface and at 444 m). Since no significant trend is seen in this data set, we did not use any low pass filter.

In Fig. 5 the values of momentum flux ($-\overline{u'w'}$) are illustrated for both periods. During the pre-storm period the momentum flux decreases with height up to 266 m, above which a slight increase occurs. The vertical structure of the momentum flux for the storm period is quite opposite to the pre-storm period, with an increase with height in the lower boundary layer and a sharp decrease in

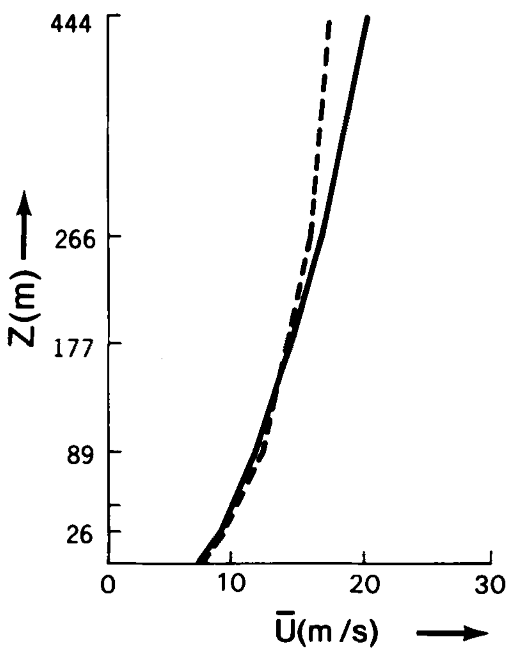

Fig. 3. Vertical profiles of mean wind component $\bar{u}$ for the periods of pre-storm (——) and storm (---).

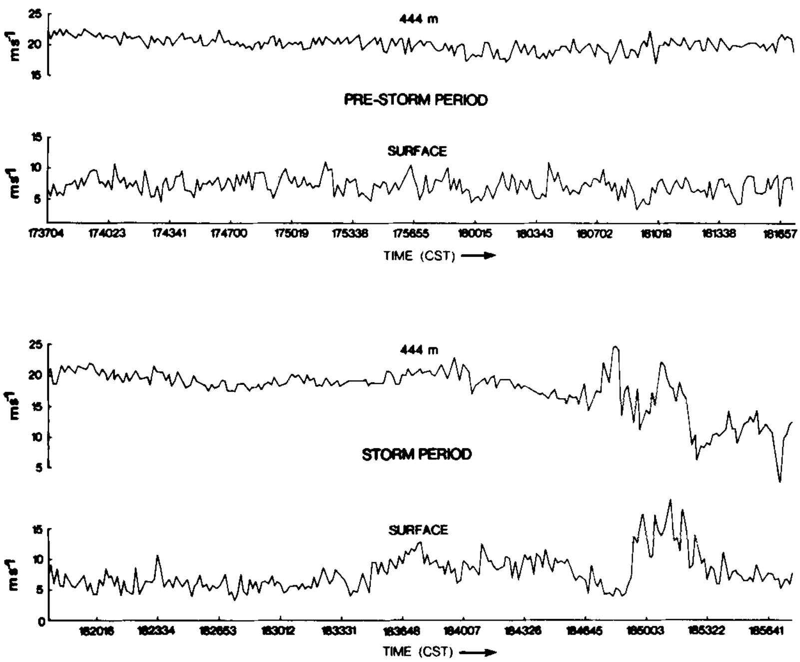

Fig. 4. Time series of observed winds at the surface and at the 444 m level. Time is in CST (hours, minutes and seconds).

the upper layer, giving a relative maximum at 266 m.

Fig. 5 also shows that during the pre-storm period the direction of momentum transport in the lower layer (below 266 m) is downward while in the upper layer it is upward even though the velocity profile in Fig. 3 indicates a positive wind shear throughout the boundary layer. Therefore, in the upper boundary layers the momentum transport is counter-gradient, implying that the large-scale motion (time scale much longer than 40 min.) is probably important for the momentum transport at upper levels. In contrast to this case during the storm period the direction of momentum transport is reversed with upward transport in the lower layer and downward transport in the upper layer. However, the countergradient transport of momentum in the lower layer during the storm period is much weaker than the down-gradient transport in the upper layers. A coupling between cloud-layer and subcloud layer seems important in momentum transports.

The height dependent turbulent heat fluxes in the subcloud layer are given in Figs. 6 and 7. It is seen that the virtual sensible heat flux evaluated by using the formula $H_S = \rho C_p \overline{w'T'}$ in Fig. 6 is almost of the same magnitude as the latent heat flux $H_L = \rho L \overline{w'q'}$ in Fig. 7 for the pre-storm period, but their contributions to the total heat flux are opposite.

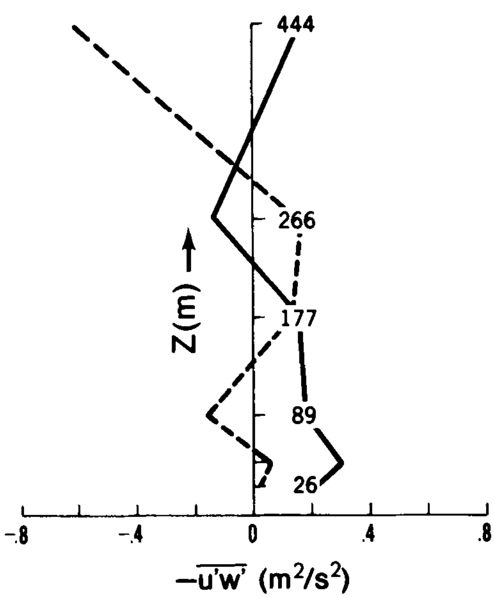

Fig. 5. Vertical profiles of momentum flux for pre-storm (——) and storm (– – –) periods.

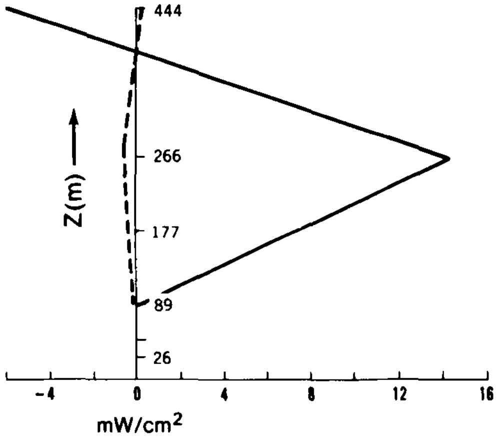

Fig. 6. Vertical profiles of the virtual turbulent heat flux for the pre-storm (——) and storm (– – –) periods.

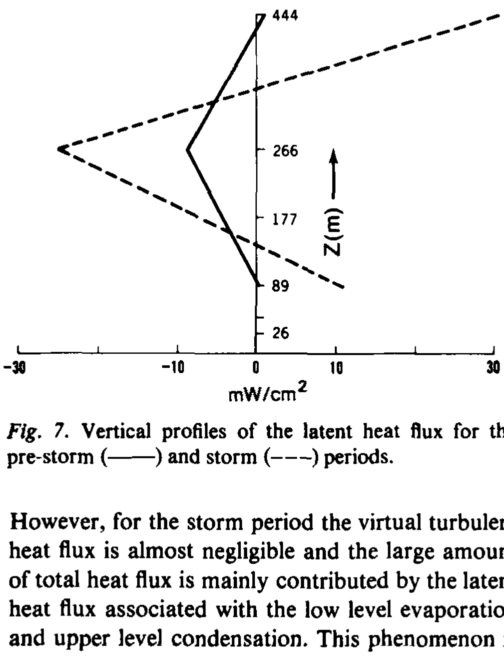

Fig. 7. Vertical profiles of the latent heat flux for the pre-storm (——) and storm (– – –) periods.

However, for the storm period the virtual turbulent heat flux is almost negligible and the large amount of total heat flux is mainly contributed by the latent heat flux associated with the low level evaporation and upper level condensation. This phenomenon is clearly seen in Fig. 2, which shows the low level moistening and upper level drying in the mean mixing ratio profile, and a large decrease of potential temperature in the lower layer and a small decrease in the upper level for the period of pre-storm to storm. The apparent decrease of the latent heat flux beneath 266 m may be attributed to the moistening during the storm period while the increase of latent heat flux above 266 m may be due to a drying effect in this layer. If the decrease of upward moisture flux in Fig. 7 is assumed to originate in the layer below 266 m, then, in the absence of a source of moisture, this layer would experience an hourly increase in mixing ratio of about 2.67 g/kg. On the other hand, above 266 m the layer of air would suffer an hourly decrease in mean mixing ratio of about 4.2 g/kg. These values are much larger than the observed mean mixing ratio change for the pre-storm to storm period in Fig. 2. Therefore, there must be a source or sink of moisture. A possible important source of moisture is the precipitation. The net virtual sensible heat output in the lower layer and its input in the upper layer as in Fig. 6 may partially balance the net downward input of latent heat in the lower layer and the net upward output in the upper layer by contributing to the energy required for the evaporation in the lower layer and the condensation in the upper layer.

4. The turbulent energy budget

We assume horizontal homogeneity and steady state flow for each period. These assumptions may be justified by the facts that the evaluated local change of turbulent kinetic energy is small compared to the other terms in the turbulent kinetic energy equation and that the main emphasis concentrates upon the relative changes that are observed between the pre-storm and storm periods. The steady-state energy budget equation (e.g. Lumley and Panofsky, 1964; Wyngaard and Cote, 1971) for each period is

$$\left(\overline{u'w'}\frac{\partial \bar{U}}{\partial z} + \overline{v'w'}\frac{\partial \bar{V}}{\partial z}\right) - \frac{g}{\bar{T}_v}\overline{w'T'_v} + \frac{\partial}{\partial z}(\overline{w'e'}) + \frac{1}{\bar{\rho}}\frac{\partial}{\partial z}(\overline{p'w'}) + \varepsilon = 0 \qquad (2)$$

where $\bar{U}$ and $\bar{V}$ are the mean velocity components and u', v' and w' are the fluctuating parts; $\bar{T}_v$ and T'_v are the mean and fluctuating virtual temperature; $\bar{\rho}$ is the mean density; p' the fluctuating pressure; g the acceleration of gravity; e' the turbulent kinetic energy $\frac{1}{2}(u'^2 + v'^2 + w'^2)$; and ε is the frictional dissipation of turbulent energy. The first two terms in Eq. (2) represent shear production (or destruction) of turbulence, the third term is buoyancy production (or destruction), the fourth is the divergence of the turbulent flux of kinetic energy (the turbulent transport), the fifth is the pressure transport, and the final term in Eq. (2) is the rate of conversion of turbulent energy into internal energy by the frictional force (or the dissipation rate). All the terms except the pressure transport and the dissipation terms in Eq. (2) are estimated from the measurements.

Fig. 8 shows profiles of the measured values of $\overline{w'e'}$ as a function of height for each period. $\overline{w'e'}$ values of the pre-storm period are much smaller than those of the storm period. During the storm period, $\overline{w'e'}$ has a negative maximum in the lower level and a positive maximum in the upper level, which indicates a transport of turbulent energy from upper levels into the lower boundary layer. In determining the actual magnitude of the turbulent kinetic energy transport, a straight line connecting two adjacent data points was used to approximate the derivative at the midpoint.

The magnitudes of various terms in the turbulent kinetic energy budget equation as a function of height are presented in Figs. 9a, b for the pre-storm and storm periods respectively. For the pre-storm period, the dominant term is shear production, especially in the lower layer. Shear production decreases rapidly with height and it appears that production of kinetic energy by buoyancy becomes important in the middle layer. However, during the storm period, the shear production term becomes unimportant and the budget is dominated by the turbulent kinetic energy transport. In the lowest layer up to 60 m, $\partial/\partial z\ (\overline{w'e'})$ is positive and above that level it is negative. This represents a transport of energy out of the upper portion of the boundary layer (presumably the cloud layer) and into the lower layer. The buoyancy production term is negligibly small and has not been plotted in Fig. 9b. Note that the shear production of turbulent kinetic energy increases with height contrary to that shown in Fig. 9a, where shear production decreases with height. A large shear production in the upper level might be caused by an increased cloud layer and the subcloud layer coupling.

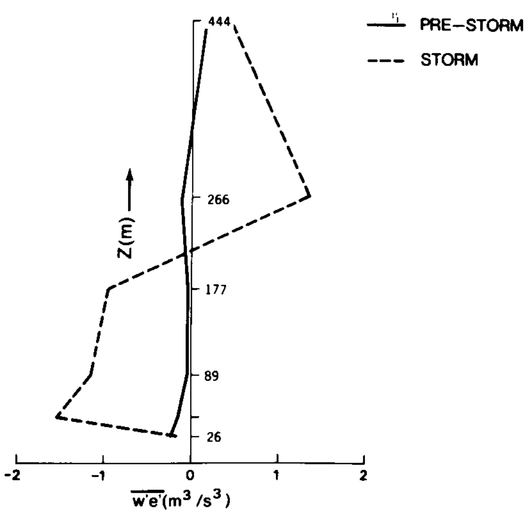

Fig. 8. Profiles of the vertical transport of turbulent kinetic energy, for the pre-storm (——) and storm (– – –) periods.

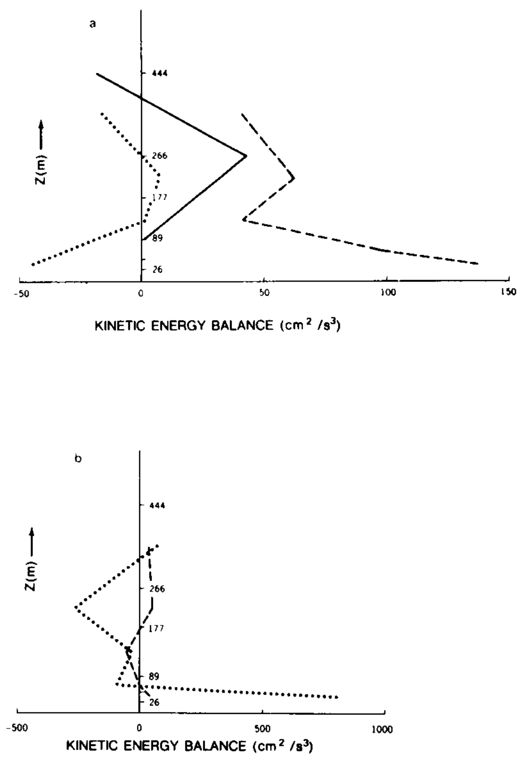

Fig. 9. The terms of the kinetic energy budget as a function of height for the (a) pre-storm and (b) storm periods. Solid line is the buoyancy generation of turbulent kinetic energy $(g/\bar{T}_v)(\overline{w'T_v'})$, dashed line is the shear generation of turbulent kinetic energy $-\overline{u'w'} \times (\partial\bar{U}/\partial z) - \overline{v'w'}\ (\partial\bar{V}/\partial z)$, and dotted line is the vertical transport of turbulent kinetic energy $-\partial(\overline{w'e'})/\partial z$.

5. Spectra and cospectra

The analysis that follows concentrates upon the relative changes that are observed between the spectra and cospectra of pre-storm and storm periods. The objective is to understand the scales of eddies that play the dominant role in the contribution of measured fluxes. The time series of horizontal wind speed, vertical velocity, virtual temperature, and mixing ratio from fixed-level tower observations were transformed into frequency space by spectrum analysis using the correlation function (Panofsky and Brier, 1968). The spectra and cospectra of the fixed-level data are presented as a function of the frequency f. When plotted in this way, the area under the curve over any frequency interval equals the contribution to the variance or covariance in that interval. The degree of freedom and the statistical confidence placed on the spectral estimates were not computed. The actual scatter in the spectral estimates is used as a measure of the statistical variability as in Pond et al. (1971).

5.1. *Pre-storm period*

During the pre-storm period the v-spectral (Fig. 10a), the u-spectral (Fig. 10b) and the w-spectral (Fig. 10c) energy in the lowest level are confined to a broad band of small scale eddies (a few hundred meters to a kilometer). There is a decrease in intensity with height. This implies convective scale motions originating near the surface.

The T_v-spectra (Fig. 10d) for the pre-storm period seem to be associated with the large-scale motions in contrast to the v-spectra where small-scale eddies mainly account for the turbulent energy variance.

The momentum flux cospectra in Fig. 10e show a scatter in the cospectral shape but there exists a general tendency for the momentum flux to decrease with height. Most of the momentum flux shown in Fig. 5 is contributed by small-scale eddies near the surface.

Fig. 10f presents the virtual heat flux spectra. There is a wide scatter in spectrum shapes in both the upper and lower levels for the pre-storm period which may imply a lower correlation between T'_v and w' within the eddies or poor organization of heat transporting eddies. Nevertheless, smaller scale eddies appear important at lower layers, while the large-scale eddies ($< 10^{-3}$ Hz) are significant at the upper levels. In contrast to this, the moisture flux spectra (Fig. 10g) contain relatively large energy at smaller scales throughout the subcloud layer.

5.2. *Storm period*

The v-fluctuation spectra for the storm period in Fig. 11a show distinct differences from the pre-storm period. The spectral amplitude is an order of magnitude greater and there is an overall increase in the energy for all scale sizes with height. The momentum transport is contributed mainly by the eddies of 20 km size in the storm period, in close agreement with the size of a thunderstorm complex. Obviously, the increased spectral amplitude is a result of thunderstorm activity, which originated at upper levels.

The u-spectra in Fig. 11b show patterns similar to v-spectra, except for stronger contributions at upper levels on a spatial scale 4–10 km and larger than 25 km. Fig. 11c presents the vertical velocity spectra. In contrast with the pre-storm period, we find a distinct spectral shift toward low frequency in the upper level of the subcloud layer and there are two well-defined spectral peaks, one at low frequency around 4.6×10^{-3} Hz (corresponding eddy size about 5 km) and another at a higher frequency. The former is attributed to the thunderstorm updrafts and/or downdrafts whose sizes are approximately the size of a thunderstorm cell. The latter may be due to buoyant eddies whose low frequency cut-off is about 10^{-2} Hz (the corresponding period is about 10 min).

The virtual temperature spectra (Fig. 11d) for the storm period show the increased dominance of scales in the range 5–10 km (corresponding spectral frequencies are 3.7×10^{-3} to 1.5×10^{-3} Hz) at the upper levels. These are related to thunderstorm updrafts and/or downdrafts. The presence of significant spectral power at lower frequency probably implies the role of scales ranging from synoptic to meso-scale processes in determining the temperature structure throughout the subcloud layer. The reduced spectral amplitude in the high frequency indicates a suppression of small-scale turbulence processes due to a strong stable stratification.

Fig. 11e shows the momentum flux spectra for the storm period. A large amount of negative momentum flux at upper levels shown in Fig. 5 is

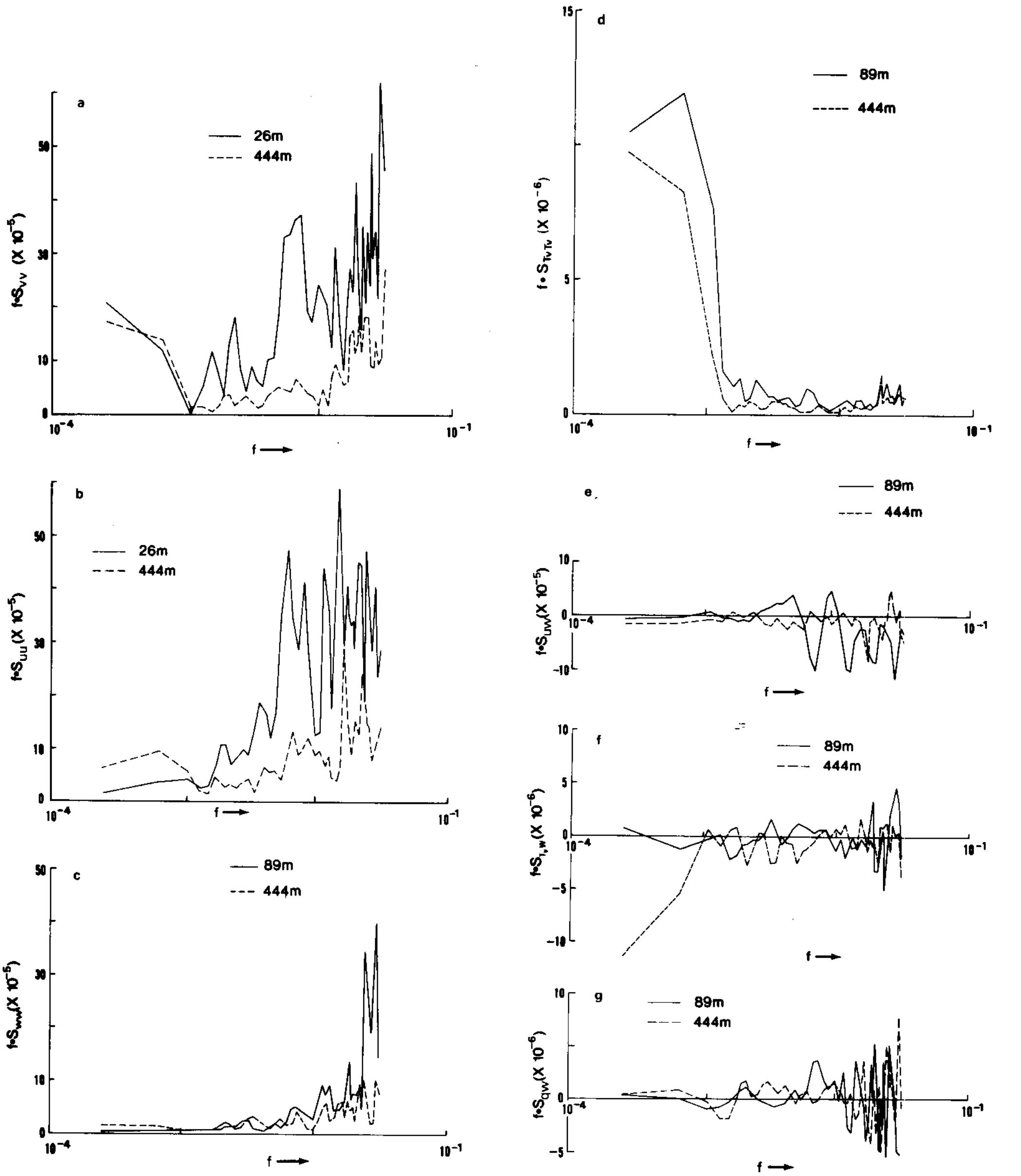

Fig. 10. Spectra of the (a) v ($m^2\ s^{-3}$), (b) u ($m^2\ s^{-3}$), (c) w ($m^2\ s^{-3}$), (d) T_v ($K^2\ s^{-1}$), (e) uw ($m^2\ s^{-3}$), (f) $T_v w$ ($K\ m\ s^{-2}$) and (g) qw ($g\ kg^{-1}\ m\ s^{-2}$) as a function of frequency (s^{-1}) for the pre-storm period.

related to thunderstorm cells whose cospectra peak is at 4.6×10^{-3} Hz (about 5 km eddy).

The virtual heat flux spectra (Fig. 11f) suggest that a well-organized storm-scale motion is the primary mechanism for the heat flux. For this storm cell ($\sim 4.2 \times 10^{-3}$ Hz) the heat flux is positive and increases with height, resulting in cooling. The cooling effects in the storm-scale are larger than the warming effects in a relatively larger scale, and consequently the temperature in the subcloud layer drops during the storm period as can be seen in Fig. 2.

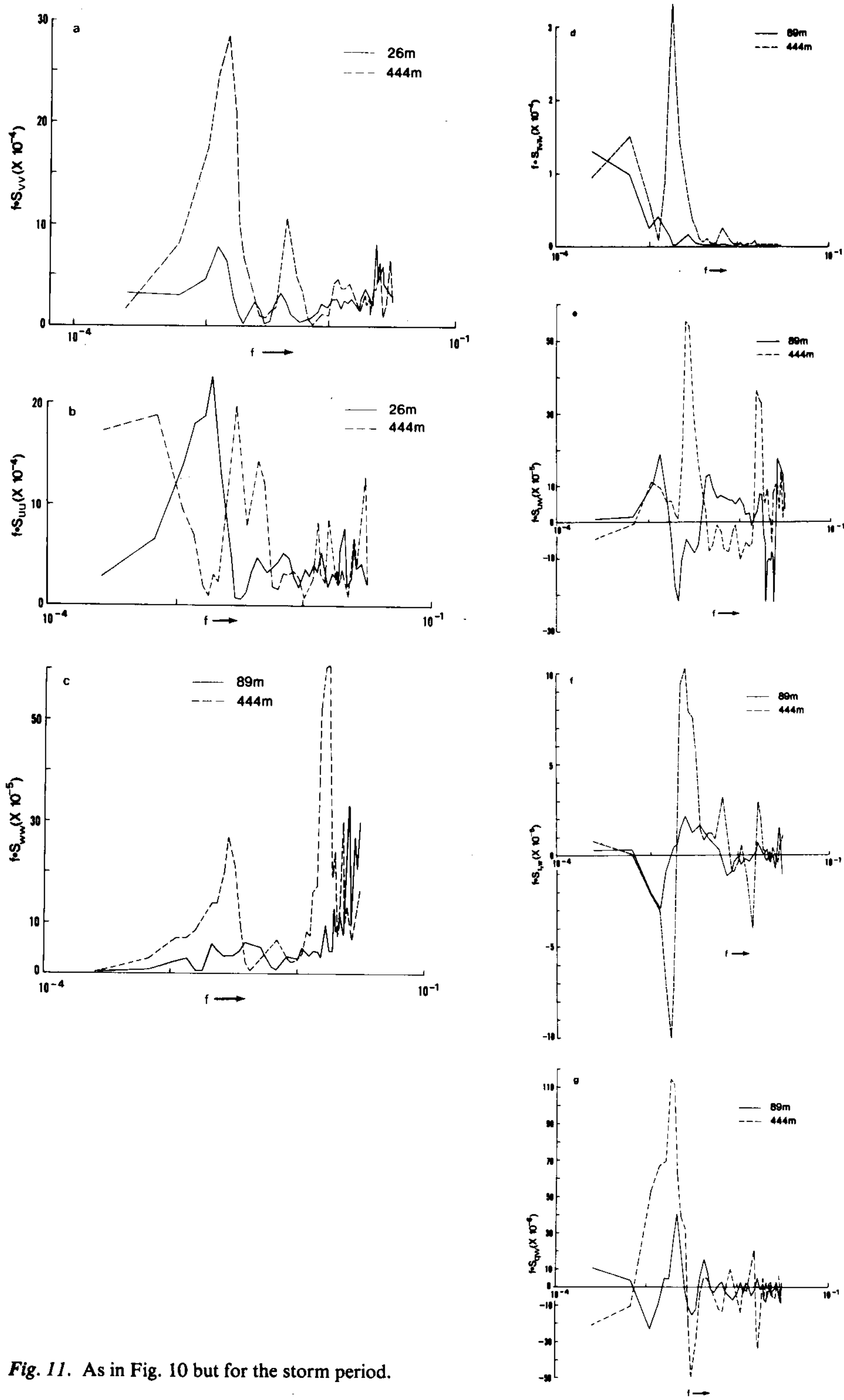

Fig. 11. As in Fig. 10 but for the storm period.

Lastly, the positive moisture flux for the storm period (Fig. 11g) associated with the large-scale motion ($<10^{-3}$ Hz) decreases with height while that for the storm-scale motion (at 3×10^{-3} Hz), which is dominant in moisture flux spectra, increases with height. This means that the large-scale motion seems to be moistening the boundary layer and the storm-scale motion to be drying it. The drying effect is stronger than the moistening effect; the result is a decrease of moisture during the storm period as seen in Fig. 2.

6. Summary and conclusion

A comparative study of the evolutionary structure of the lower boundary layer between the pre-storm and storm periods has been investigated using meteorological tower data. Analyses include the mean and turbulent quantities of velocity components, temperature, mixing ratio and the fluxes of momentum, heat and moisture.

Significant structural changes in the lower boundary layer were noted as the storm passed. The tower experienced a significant temperature drop at the lower boundary layer and a slight drop at the upper boundary layer. Consequently, the boundary layer was more stably stratified. A large temperature drop at the lower layer was due to the evaporative cooling; the transport of turbulent heat flux upward and the cold downdrafts were associated with precipitation. On the other hand, because cold downdrafts from the cloud layer above were compensated by latent heat release and by turbulent heat fluxes transported upward from the lower levels, cooling in the upper boundary layer was relatively small.

The mean horizontal wind also showed a significant change during the storm period. Strong mixing above 89 m and a weak mixing of turbulent momentum beneath 89 m was associated with a strong stratification below 89 m (see Fig. 2). The observed low-level wind maximum (not presented here) may be attributed to this mixing process.

Although the turbulent kinetic energy budget was not completed due to the limitation of data resolution, it appeared that the dominant term in the turbulence energy budget was the shear generation term for the pre-storm period. In contrast, during the storm period the largest term was the turbulent transport term.

During the pre-storm small-scale turbulent motions that originated from the surface determined the structure of momentum and moisture fluxes. On the other hand, the temperature spectra and the virtual heat flux apparently were determined by the prevailing large-scale motions. During the storm period the influence of thunderstorm-scale motion on the momentum, heat, moixture fluxes and wind, temperature, and moisture spectra was so strong that the contributions of other scales of motion to the total was negligible, except for the vertical velocity spectra, where the contribution of buoyant eddies was significant. This was particularly true in the upper levels of the boundary layer. The structure of the boundary layer during the storm period was mainly determined by the fluxes originating from the cloud layer or upper level boundary layer on the thunderstorm-scale instead of by surface originated fluxes associated with small-scale turbulence, which was the case in the pre-storm or mixed-layer boundary layer. The small-scale turbulences were greatly suppressed by the stable stratification.

The total heat fluxes in the boundary layer were primarily determined by the latent heat fluxes. The sensible heat flux was negligible compared to the latent flux except in the pre-storm period, when both fluxes were comparable.

The most notable findings in this case study are the following: (1) in the pre-storm period, the boundary layer structure was controlled by the surface layer fluxes of heat and momentum, similar to a mixed layer situation (Tennekes, 1973; Ball, 1960; Carson, 1973); (2) in the storm-period, the subcloud layer structure was mainly determined by forcing from the cloud layer on a storm-scale, in general agreement with others (Echternacht and Garstang, 1976).

7. Acknowledgements

The authors wish to thank Dr. David W. Martin, Space Science and Engineering Center, UW-Madison for reading the manuscript and offering valuable comments. The tower data used in this research were furnished by the National Severe Storms Laboratory, Oklahoma. Financial support came from the National Science Foundation under Grant nos. ATM-77-24842 and ATM-8109144 and the Graduate School, University of Wisconsin-Milwaukee.

REFERENCES

Ball, F. K. 1960. Control of inversion height by surface heating. *Quart. J. Roy. Meteorol. Soc. 86*, 483–494.

Businger, J. A., Wyngaard, J. C., Izumi, Y. and Bradley, E. F. 1971. Flux-profile relationships in the atmospheric surface layer. *J. Atmos. Sci. 28*, 181–189.

Carson, D. J. 1973. The development of a dry inversion-capped convectively unstable boundary layer. *Quart. J. Roy. Meteorol. Soc. 99*, 450–467.

Carter, J. K. 1970. The meteorologically instrumented WKY-TV tower facility. NOAA Tech Memo. ERLTM-NSSL-50, COM-71-00108, 18 pp.

Charba, J. 1974. Application of gravity current model to analysis of squall-line gust front. *Mon. Wea. Rev. 102*, 140–156.

Colmer, M. G. 1971. *On the character of thunderstorm gust fronts*. Roy. Aircraft Establishment, Bedford, England, 11 pp.

Coulman, C. E. and Warner, J. 1977. Temperature and humidity structure of the sub-cloud layer overland. *Bound. Layer Meteorol. 11*, 467–484.

Echternacht, K. L. and Garstang, M. 1976. Changes in the structure of the tropical sub-cloud layer from the undisturbed to disturbed states. *Mon. Wea. Rev. 104*, 407–417.

Goff, R. C. and Zittel, W. D. 1974. The NSSL/WKY-TV tower data collection program: April-July 1972. NOAA Tech. Memo. ERL NSSL-68, COM-74-11334, 48 pp.

Lenschow, D. H. 1970. Airplane measurements of planetary boundary layer structure. *J. Appl. Meteorol. 9*, 874–884.

Lumley, J. L. and Panofsky, H. A. 1964. *The structure of atmospheric turbulence*. New York, Interscience, 239 pp.

Mahrt, L. and Lenschow, D. H. 1976. Growth dynamics of the convectively mixed layer. *J. Atmos. Sci. 33*, 41–51.

Panofsky, H. A. and Brier, G. W. 1968. *Some applications of statistics to meteorology*. University Park Pennsylvania, 224 pp.

Park, S.-U. and Sikdar, D. N. 1980. An application of a simple diagnostic cloud model to the May 20, 1977 storms over the Oklahoma meso-network. *Tellus 32*, 326–339.

Pennell, W. T. and LeMore, M. A. 1974. An experimental study of turbulence structure in the fair-weather trade wind boundary layer. *J. Atmos. Sci. 31*, 1308–1323.

Pond, S., Phelps, G. T. and Paquin, J. E. 1971. Measurements of the turbulent fluxes of momentum, moisture and sensible heat over the ocean. *J. Atmos. Sci. 28*, 901–917.

Tennekes, H. 1973. A model for the dynamics of the inversion above a convective boundary layer. *J. Atmos. Sci. 30*, 558–567.

Wyngaard, J. C. and Cote, O. R. 1971. The budgets of turbulent kinetic energy and temperature variance in the atmospheric surface layer. *J. Atmos. Sci. 28*, 190–201.